Nanoscale

Helically Aligned Fused Carbon Hollow Nanospheres with Chiral Discrimination Ability

Journal:	*Nanoscale*
Manuscript ID	NR-ART-12-2021-007971.R1
Article Type:	Paper
Date Submitted by the Author:	28-Jan-2022
Complete List of Authors:	Maruyama, Jun; Osaka Research Institute of Industrial Science and Technology, Research Division of Environmental Technology Maruyama, Shohei; Osaka Research Institute of Industrial Science and Technology, Kashiwagi, Yukiyasu; Osaka Municipal Technical Research Institute, Watanabe, Mitsuru; Osaka Research Institute of Industrial Science and Technology, Electronic Materials Research Division Shinagawa, Tsutomu; Osaka Research Institute of Industrial Science and Technology, Electronic Materials Research Division Nagaoka, Toru; Osaka Research Institute of Industrial Science and Technology, Research Division of Materials Science and Engineering Tamai, Toshiyuki; Osaka Research Institute of Industrial Science and Technology, Morinomiya Center Ryu, Naoya; Kumamoto Industrial Research Institute, Materials Development Department Matsuo, Koichi; Hiroshima Univ Ohwada, Mao; Tohoku University, Institute of Multidisciplinary Research for Advanced Materials Chida, Koki; Tohoku University, Yoshii, Takeharu; Tohoku University, Institute of Multidisciplinary Research for Advanced Materials Nishihara, Hirotomo; Tohoku University, Institute of Multidisciplinary Research for Advanced Materials Tani, Fumito; Kyushu University, Institute for Materials Chemistry and Engineering Uyama, Hiroshi; Osaka Univerisity,

ARTICLE

Helically Aligned Fused Carbon Hollow Nanospheres with Chiral Discrimination Ability

Received 00th January 20xx,
Accepted 00th January 20xx

DOI: 10.1039/x0xx00000x

Jun Maruyama,*[a] Shohei Maruyama,[a] Yukiyasu Kashiwagi,[a] Mitsuru Watanabe,[a] Tsutomu Shinagawa,[a] Toru Nagaoka,[a] Toshiyuki Tamai,[a] Naoya Ryu,[b] Koichi Matsuo,[c] Mao Ohwada,[d] Koki Chida,[e] Takeharu Yoshii,[e] Hirotomo Nishihara,[d,e] Fumito Tani,[f] and Hiroshi Uyama[g]

While the functions of carbon materials with precisely controlled nanostructures have been reported in many studies, their chiral discriminating abilities have not been reported yet. Herein, chiral discrimination is achieved using helical carbon materials devoid of chiral attachments. A Fe_3O_4 nanoparticle template with ethyl cellulose (carbon source) is self-assembled on dispersed multiwalled carbon nanotubes (MWCNTs) fixed in a lamellar structure, with helical nanoparticle alignment induced by the addition of a binaphthyl derivative. Carbonization followed by template removal produces helically aligned fused carbon hollow nanospheres (CHNSs) with no chiral molecules left. Helicity is confirmed using vacuum-ultraviolet circular dichroism spectroscopy. Chiral discrimination, as revealed by the electrochemical reactions of binaphthol and a chiral ferrocene derivative in aqueous and nonaqueous electrolytes, respectively, is attributable to the chiral space formed between the CHNS and MWCNT surfaces.

Introduction

Carbon materials are typically synthesized from inexpensive organic compounds using high-temperature heat treatment in inert atmospheres. The resulting polyaromatic ring generation, fusion, and π-conjugation development impart high chemical stability and electron conductivity, which are advantageous for electrode materials. However, nanostructure tuning is difficult because C–C bond formation occurs randomly during heat treatment.

Various techniques have been developed to precisely control the nanostructure of carbon materials, such as the thermally induced phase separation of carbon precursor solutions followed by carbonization.[1] Recently, selective C–C bond formation in organic crystals with rigid porphyrin rings and reactive alkynyl substituents was used to synthesize 3D-ordered carbonaceous frameworks.[2] The most effective technique is the template method, wherein composites are formed between the raw materials and templates that guide the morphology of the carbonaceous phase during heat treatment.[3] Carbon nanomaterials with 1D-, 2D-, and 3D-ordered structures, including tubular,[4] fibrous,[5] graphene-like,[6] inverse opal,[7] and gyroid-like structures,[8] have been synthesized and successfully applied as electrodes in many devices.[9,10]

New helical morphologies have been realized for carbon materials in the past 15 years. Chiral compounds, including nematic liquid crystals, amphiphiles, and gelators, have been used as templates to generate helical carbon materials derived from polyacetylene, polypyrrole, and polymeric silsesquioxanes, respectively.[11–13] Recently, we synthesized cylindrical carbon with honeycomb-like helically aligned pores by self-assembling 40 nm polystyrene nanoparticles (NPs) as a pore formation template with fructose as a carbon source as well as a chiral inducer.[14] These helical carbon materials exhibited optical activity, as observed by circular dichroism (CD) measurements, but no chirality-based functions were found. No studies have reported interactions between chiral molecules and helical carbon materials, which may be due to size mismatch; for example, alanine[15] and 1,1′-bi-2-naphthol (BINOL)[16] have sub- to one-nanometer sizes, and helical carbon has a diameter of at least ~100 nm.

Chiral discrimination remains challenging because enantiomers have identical chemical and physical properties. Conventionally, materials with chiral discrimination ability are synthesized by attaching chiral molecules or polymers as hosts that interact with chiral guest molecules.[17–22] The modification of carbon electrode surfaces with chiral compounds has also been reported.[23] However, these materials potentially suffer from

---

[a] Osaka Research Institute of Industrial Science and Technology
1-6-50, Morinomiya, Joto-ku, Osaka 536-8553, Japan
E-mail: maruyama@omtri.or.jp
[b] Kumamoto Industrial Research Institute
3-11-38, Higashimachi, Higashi-ku, Kumamoto 862-0901, Japan
[c] Hiroshima Synchrotron Radiation Center, Hiroshima University
2-313 Kagamiyama, Higashi-Hiroshima 739-0046, Japan
[d] Advanced Institute for Materials Research, Tohoku University
2-1-1, Katahira, Aoba-ku, Sendai, 980-8577, Japan
[e] Institute of Multidisciplinary Research for Advanced Materials, Tohoku University
2-1-1, Katahira, Aoba-ku, Sendai, 980-8577, Japan
[f] Institute for Materials Chemistry and Engineering, Kyushu University
744, Motooka, Nishi-ku, Fukuoka 819-0395, Japan
[g] Department of Applied Chemistry, Graduate School of Engineering, Osaka University
2-1, Yamadaoka, Suita 565-0871, Japan

† Footnotes relating to the title and/or authors should appear here.

Electronic Supplementary Information (ESI) available: [details of any supplementary information available should be included here]. See DOI: 10.1039/x0xx00000x

host-compound detachment and decomposition under harsh conditions. In contrast, it has recently been reported that chiral imprinting is a useful technique for forming inorganic matrices with nanopores or morphologies that reflect the spatial arrangement of an enantiomer, which facilitates preferential interactions with the same enantiomer.[24–27]

In this study, inspired by the fabrication of molecule-sensitive nanostructures, we developed a new helical carbon material without attached chiral compounds with an appropriate scale for chiral discrimination and investigated the formation mechanism, optical characteristics, and electrochemical functions thereof. Helically aligned fused carbon hollow nanospheres (CHNSs) were formed on multiwalled carbon nanotubes (MWCNTs) in the presence of a binaphthyl derivative (Fig. 1). The space between the CHNS and MWCNT surfaces was enantiomeric, i.e., not superimposable on the mirror-image counterpart because the right-handed (RH) and left-handed (LH) helices of the aligned CHNSs possessed different short and long pitches (Fig. S1). As an electrode material, the intrinsic defects in the CHNS shell and the hollow space enabled mass transfer to the chiral space from the bulk electrolyte. Notably, BINOL with opposite axial chirality to the binaphthyl derivate used to induce chirality yielded higher electrochemical oxidation currents than BINOL with identical spatial arrangement, indicating that this helical carbon material has a novel chiral discrimination mechanism.

Results and discussion

Self-Assembly of Fe_3O_4 NPs on MWCNTs with a Carbon Source and Chiral Inducer

The synthesis of helically aligned fused CHNSs on MWCNTs is shown schematically in Fig. 1. A carbon shell was formed around the template (Fe_3O_4 NPs, 5 nm in diameter), and a molecular-level chiral space was created between the carbon shell surface and the MWCNTs (Fig. S1). The advantages of using Fe_3O_4 NPs include the availability of homogeneous nano-sized particles, their shape retention ability at temperatures above those required for carbonization, and their easy removability with common acids.

Two helical structures with opposite chiralities were fabricated using (*S*)- and (*R*)-binaphthyl derivatives (2,2′-bis(methoxymethoxy)-1,1′-binaphthyl) as chiral inducers. Highly ordered 3D mesoporous carbon materials have been previously synthesized through slow solvent evaporation using self-assembled Fe_3O_4 NPs coated with oleic acid as a carbon source.[28] Helical superstructures of cubic Fe_3O_4 NPs have also been reported.[29] However, these methods produced closely packed Fe_3O_4 NP assemblies with no hollow spaces. Thus, we added another carbon source to form a carbon shell around the Fe_3O_4 NPs and generate a chiral space. Ethylcellulose (EC) was chosen as the carbon source owing to its low cost and good

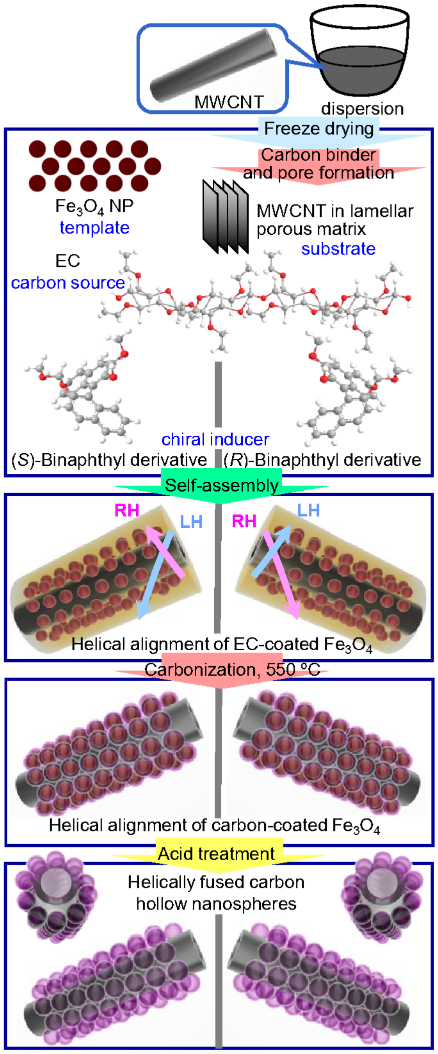

Fig. 1. Synthesis of helically aligned fused CHNSs on MWCNTs. An aqueous MWCNT dispersion with sodium alginate and poly(ethylene oxide)/poly(propylene oxide) triblock copolymer as a carbon binder precursor and pore-forming agent, respectively, is freeze-dried and heat-treated at 800 °C to form a lamellar porous MWCNT substrate. A mixture of dispersed Fe_3O_4 NPs, ethylcellulose (EC), and 2,2′-bis(methoxymethoxy)-1,1′-binaphthyl self-assembles on MWCNTs fixed in the lamellar porous matrix. Subsequent heat treatment at 550 °C forms helically aligned fused carbon-coated Fe_3O_4. Acid treatment then removes Fe_3O_4 to obtain CHNSs. The arrows show left-handed (LH) and right-handed (RH) helices. Long-pitch RH and short-pitch LH helices are generated from the mixture with the *R*-binaphthyl derivative (right). Long-pitch LH and short-pitch RH helices are generated from the mixture with the *S*-binaphthyl derivative (left).

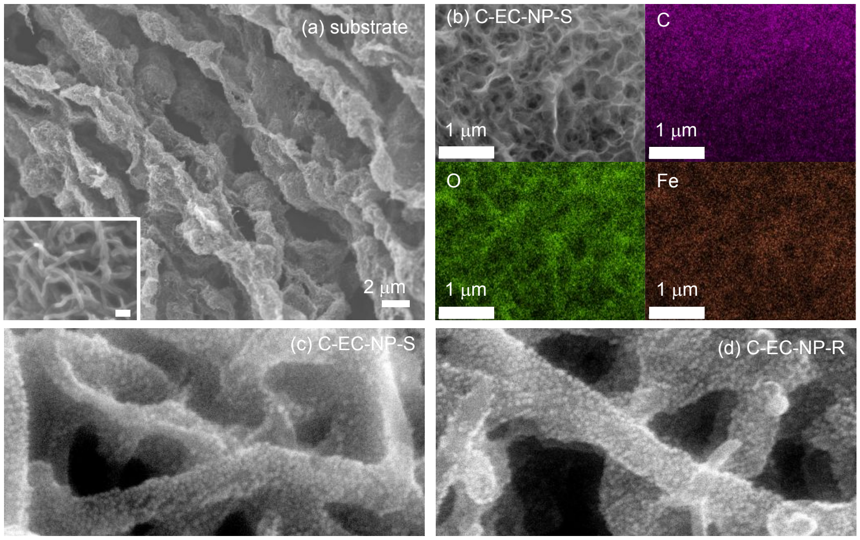

Fig. 2. FESEM image of MWCNT substrate (a), FESEM-EDX elemental mapping images of C-EC-NP-S (b), FESEM images of C-EC-NP-S (c), and C-EC-NP-R (d). The inset in (a) shows a magnified view of the sheet surface in the lamellar structure (scale bar, 100 nm).

solubility in organic solvents suitable for evaporation-induced NP assembly.

Generating an ordered structure from multiple nanomaterials is complicated and influenced by subtle condition changes.[30] This complexity is a potential problem in forming helically aligned CHNSs on MWCNTs. Indeed, a preliminary experiment showed that the simple mixing of dispersed MWCNTs and the Fe_3O_4 NP dispersion with EC followed by solvent evaporation resulted in an inhomogeneous composite (Fig. S2). We overcame this difficulty by simplifying the assembly process. Instead of multicomponent conditions, wherein all of the multiple nanomaterials are dispersed within a single liquid phase, the MWCNTs in a dispersed state were fixed in a highly porous substrate, onto which the Fe_3O_4 NPs with EC and the chiral inducer could be effectively self-assembled. The ice-template method was employed to form a lamellar structure with sufficient macroporosity[31] (Fig. 2a) to supply the Fe_3O_4 NPs to the MWCNT surface. An aqueous MWCNT dispersion was prepared with sodium alginate as a carbon binder precursor to fix MWCNT and poly(ethylene oxide)/poly(propylene oxide) triblock copolymer (Pluronic F127) as a pore-forming agent to form pores in the lamellar sheet. The dispersion was freeze-dried and heat-treated at 800 °C to form a lamellar porous MWCNT substrate.

The synthesis of helically aligned fused CHNSs on MWCNTs comprised three steps: (1) immersion of the MWCNT substrate in a mixture of dispersed Fe_3O_4 NPs, EC, and the chiral inducer, followed by solvent evaporation to induce self-assembly and form the precursor; (2) heat treatment at 550 °C in an Ar atmosphere for carbonization; and (3) acid treatment to remove the Fe_3O_4 template. The precursors obtained using the (*R*)-binaphthyl derivative, (*S*)-binaphthyl derivative, and no chiral inducer are labeled EC-NP-R, EC-NP-S, and EC-NP, respectively. The corresponding carbonized and acid-treated samples are labeled with C- and -a, respectively (for example, C-EC-NP-R and C-EC-NP-R-a). Fig. 2b shows the elemental mapping images obtained by field emission scanning electron microscopy (FESEM)–energy-dispersive X-ray spectroscopy (EDX). The observation of uniform distributions of Fe and O along the MWCNTs indicated successful Fe_3O_4 loading.

Helical Alignment of Fused CHNSs

FESEM images of C-EC-NP-R and C-EC-NP-S (Fig. 2c and d; for magnified views, see Fig. S3) illustrate helically aligned white dots attributed to Fe_3O_4 NPs on the MWCNT surface. Two forms with opposite helicities were achieved using the stereoisomers of the chiral inducer, although some disorder was detected, which was attributed to MWCNT bending. The transmission electron microscopy (TEM) image of C-EC-NP (Fig. 3a), which was prepared without a chiral inducer, shows Fe_3O_4 NPs densely loaded on MWCNTs without noticeable helicity, whereas the TEM images of C-EC-NP-R and C-EC-NP-S show helical alignments (Fig. 3b and c). The removal of Fe_3O_4 by acid treatment left CHNSs on the MWCNTs (Fig. 3d, e, and f). The helical alignment of the CHNSs was also observed in C-EC-NP-S-a and C-EC-NP-R-a.

Studies on helical carbon materials have shown that positive and negative peaks in the CD spectra correspond to LH and RH helical structures, with the peak position modulated by the helical pitch.[12–14] The disorder was observed in the helical alignment in the FESEM and TEM images. Therefore, we recorded the CD spectra of the carbon samples obtained in this study to confirm the helicity. The CD spectra were recorded in the vacuum-ultraviolet (VUV) region because these helical carbon materials have smaller pores and cylindrical diameters, and consequently, shorter helical pitches than those of previously reported materials exhibiting CD peaks in the visible-light region.[14]

Fig. 4a and b show the VUVCD and absorption spectra, respectively, of substrate-a, C-EC-NP-a, C-EC-NP-R-a, and C-EC-NP-S-a. The absorbance of each sample increased at wavelengths lower than 180 nm, which was attributed to the σ–

σ* transition.[32] The small peak observed at approximately 195 nm for substrate-a might be due to the π-plasmon absorbance of the MWCNTs.[33,34] No appreciable CD signals were observed in the spectra of substrate-a and C-EC-NP-a, indicating the absence of helicity or that the RH/LH helicity ratio of each pitch was near unity. In contrast, positive and negative signals exceeding a noise level of ±0.7 mdeg were observed for C-EC-NP-S-a and C-EC-NP-R-a, respectively. Although the intensities were moderate, these signals demonstrated the chirality of the fused CHNSs on MWCNTs synthesized with the chiral inducer. The correlation between the sign of the CD signal and the helicities of C-EC-NP-S-a and C-EC-NP-R-a was in agreement with those reported previously.[12,13] Despite the low intensity at the CD spectra of C-EC-NP-S-a and C-EC-NP-R-a, the reproducibility was confirmed by the nearly identical spectra for the samples independently synthesized by the same method (Fig. S4a). The deviation from the mirror-image spectra might be attributable to marginal interaction between the chiral inducer and optically active EC, as discussed in the following section. Numerous CD spectra have been reported for helical silica[35] and Au helical nanostructures.[36] In contrast, CD data for helical carbon materials are limited, and the origins of the CD signals are presently unknown. At least, possibility of attributing the origin to any chiral molecule eluted in the dispersion used for the sample fixing was excluded because the CD spectrum for the supernatant obtained by removing C-EC-NP-S-a from its dispersion showed no CD signal (Fig. S4b). Further investigations are required to clarify the origins of these signals in helical carbon materials. In addition, the method for fixing the sample in the CD measurement cell must be optimized to improve signal intensity.

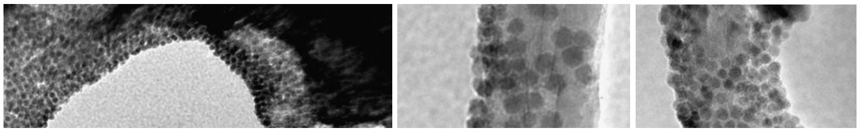

Fig. 3. TEM images of CHNSs on MWCNTs. CHNSs before (C-EC-NP (a), C-EC-NP-S (b), and C-EC-NP-R (c)) and after acid treatment (C-EC-NP-a (d), C-EC-NP-S-a (e), and C-EC-NP-R-a (f)).

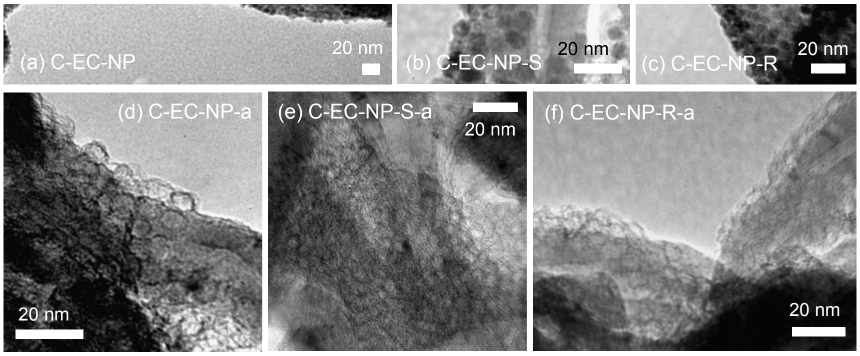

X-ray photoelectron spectroscopy (XPS) analysis showed higher O 1s peak intensity for the CHNS-attached MWCNTs than for the MWCNTs, indicating that the CHNSs were composed of amorphous carbon (Fig. 4c). Wide-scan XPS spectra (Fig. S5) confirmed that Fe_3O_4 was completely removed by the acid treatment. The Raman spectra of the CHNS-attached MWCNTs were similar to those typically observed for amorphous carbon (Fig. 4d),[37,38] with some influence of the MWCNT substrate owing to the thinness of the CHNS carbon shell. Carbonized EC and EC-NP-R, which were formed without using the MWCNT substrate, showed typical Raman spectra of amorphous carbon (Fig. S6) without the influence of the MWCNT substrate, thus supporting the XPS results. The N_2 adsorption isotherms of the CHNS-attached MWCNTs and the MWCNTs were similar (Fig. 4e). The specific surface areas of MWCNTs, C-EC-NP-a, C-EC-NP-R-a, and C-EC-NP-S-a were 112, 135, 199, and 164 $m^2\ g^{-1}$, respectively. A difference of approximately 40 $m^2\ g^{-1}$ between the specific surface areas of the CHNS-attached MWCNTs and the MWCNTs was expected based on the contents of the starting mixture, assuming that the 5-nm Fe_3O_4 NPs were spherical. Although the observed increase in the specific surface area varied from the predicted value to some extent, they can be attributed to the attachment of CHNSs on MWCNTs. No distinct peaks were observed in the pore size distributions; nevertheless, it should be noted that nanopores (pore diameter < 2 nm) were developed.

Formation Mechanism of Helically Aligned Fused CHNSs

The thermal decomposition behavior and carbonization behavior of the components used for CHNS synthesis were examined. EC was optically active, as revealed by CD measurements; however, the optical activity decreased and was eventually eliminated by carbonization (Fig. S7). The strong CD signal corresponding to the binaphthyl derivative at 215–250 nm was also observed in its mixtures with EC (Fig. S7). This signal disappeared as the heat-treatment temperature increased, which indicated that the chiral inducer lost its function during the carbonization step. Thus, the helical alignment of the Fe_3O_4 NPs was generated in the self-assembly step during solvent evaporation.

Upon dropping the Fe_3O_4 NP dispersion in toluene onto the TEM grid and drying, a close-packed arrangement of Fe_3O_4 NPs was observed (Fig. S8). The mixture of Fe_3O_4 NPs and EC used for

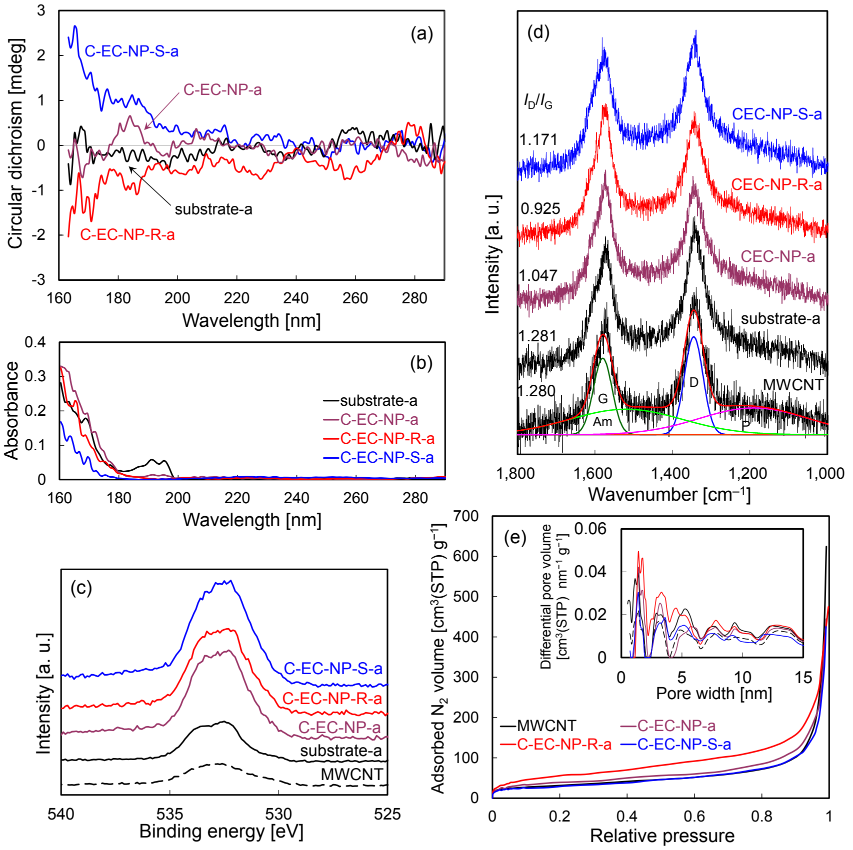

preparing the EC-NP precursor also generated a close-packed arrangement (Fig. S8). The distance between the particle centers increased marginally from 8.31 to 8.84 nm (averaged over 100 recorded values) in the presence of EC. This increase is insufficient to accommodate EC in the space between the self-assembled Fe_3O_4 NPs, indicating that the majority of EC is situated outside of the self-assembled Fe_3O_4 NP layer on the MWCNTs. The FESEM images of the EC-NP-R and EC-NP-S precursors confirm thick EC coverage on the MWCNTs (Fig. S9). Considering the potentially favorable interaction between the naphthyl groups of the binaphthyl derivative and the MWCNT surface,[39] it is reasonable to assume that the Fe_3O_4 NPs self-assembled on the chiral-inducer-adsorbed MWCNT surface, which caused the helical alignment of the close-packed NPs. Interference by optically active EC could be marginal because its presence inside the close-packed NP layer was limited. During heat treatment, the majority of EC could penetrate the space between the NPs by softening and partial melting, with subsequent decomposition and carbonization generating a carbon shell surrounding the NPs and possibly also the MWCNTs. Thus, a molecular-level chiral space was created between the carbon shell surface and the cylindrical surface of the carbonized-EC-coated or bare MWCNTs.

Thermogravimetry coupled with differential scanning calorimetry and mass spectrometry (TG-DSC-MS) simultaneously demonstrated the mass loss, heat flow, and decomposition-derived gaseous species. The decomposition of each component in the starting mixture (EC, Fe_3O_4 NPs with dispersant, and the binaphthyl derivative) occurred at 300–400 °C, 150–500 °C, and above 200 °C, respectively (Fig. S10–S13). However, significantly altered behavior was observed during the heat treatment of mixtures, which was attributed to interactions between the mixture components. The decomposition behavior of mixtures of EC, Fe_3O_4 NPs, and binaphthyl derivatives was similar to that of the mixture of EC and Fe_3O_4 NPs (Fig. S14–S18). Furthermore, the gaseous species emitted during the decomposition of the EC and Fe_3O_4 NP mixture were detected in different temperature ranges than those emitted during the decomposition of each component, indicating the occurrence of an EC-NP interaction and confirming the feasibility of carbon shell formation around the Fe_3O_4 NPs. Similarly, interactions between EC and the binaphthyl derivatives were indicated by changes in the decomposition behavior of the mixtures. The gaseous species observed up to 600 °C during the decomposition of the binaphthyl derivatives disappeared after the derivatives were mixed with EC and Fe_3O_4 NPs with dispersant, which indicated that the chiral inducer decomposed completely during heat treatment and was absent from the CHNS-attached MWCNTs.

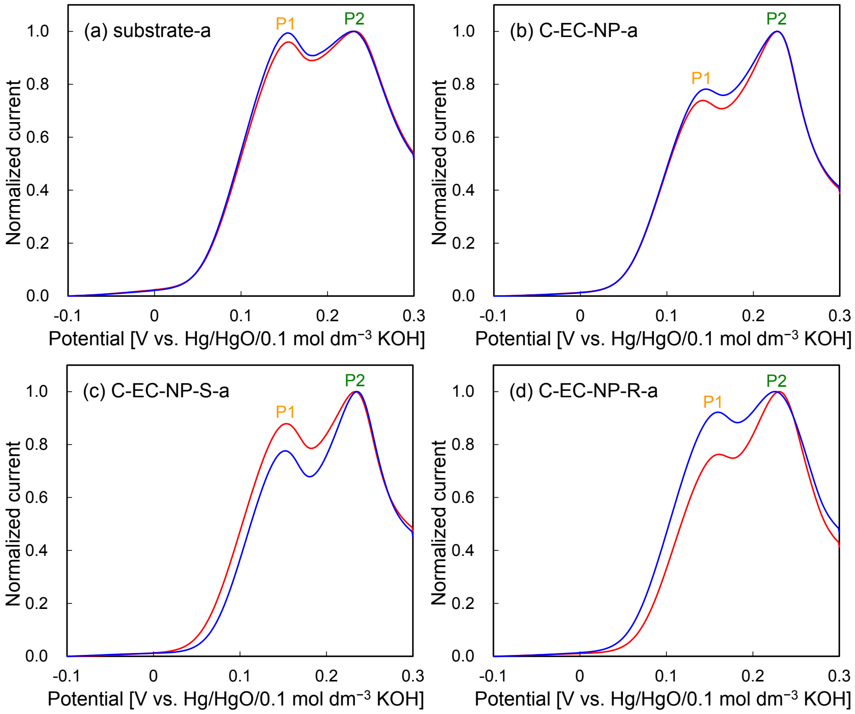

Fig. 5. Helically aligned fused CHNSs as chiral electrodes in an aqueous system. Linear sweep voltammograms of substrate-a (a), C-EC-NP-a (b), C-EC-NP-S-a (c), and C-EC-NP-R-a (d) electrodes in 1 mmol dm^{-3} (*R*)- (—) and (*S*)-BINOL (—) dissolved in Ar-saturated 0.1 mol dm^{-3} KOH aqueous solution at 25 °C (sweep rate: 10 mV s^{-1}). The current was normalized by the maximum current of P2. A typical non-normalized linear sweep voltammogram is shown in Fig. S21.

Fig. 4. Characteristics of helically aligned fused CHNSs on MWCNTs. CD spectra (a), absorption spectra (b), O 1s XPS spectra (c), Raman spectra (d), and N_2 adsorption isotherms at −196 °C (e) of MWCNTs, substrate-a, C-EC-NP-a, C-EC-NP-R-a, and C-EC-NP-S-a. The inset in (e) shows the pore size distributions. The O 1s XPS peak intensity in (c) was normalized by the area of the C 1s XPS peak. The Raman spectra in (d) were deconvoluted into four components: graphitic peak (G peak) at 1600–1580 cm^{-1}, disorder peak (D peak) at 1355–1345 cm^{-1}, a peak ascribed to amorphous carbon (Am peak) at 1525–1490 cm^{-1}, and a peak ascribed to sp^3-bonded carbon atoms (P peak) at 1190–1150 cm^{-1}.

Helically Aligned Fused CHNSs as Chiral Electrodes

The CHNS-attached MWCNT samples were fixed between a porous carbon paper sheet and expanded graphite foil backing as a sample holder to form an electrode (Fig. S19). A pair of enantiomers, (*R*)-(+)- and (*S*)-(−)-BINOL, dissolved in an alkaline electrolyte[40] was used as a chiral guest to evaluate the performance of the helically aligned fused CHNSs as an electrode material for chiral discrimination. This chiral guest was selected because it exhibits reactivity on carbon electrodes without requiring additional catalyst within a moderate potential range, wherein carbon electrodes have been reported to perform stably in alkaline electrolytes.[41,42]

The electrochemical oxidation of BINOL on the carbon electrodes was similar to that of hydroquinone (HQ) and catechol (CC). The position of the oxidation peak in the current–potential curve depended on the properties of the carbon surface, and surface activation by roughening and functional-group enrichment shifted the peak to a lower potential (Fig. S20).[43,44] The current–potential curve for (*R*)-BINOL on the sample holder comprised two peaks at low and high potentials, labeled P1 and P2, respectively. P2 was dominant (Fig. S20), indicating that the surface consisted of two areas having different activities and that most of the surface was less active. The development of P1 was observed on the electrodes containing CHNS-attached MWCNTs as well as substrate-a (Fig. 5 and S21). Based on a previous study showing that MWCNTs are active for HQ and CC oxidation,[45] P1 and P2 were attributed to BINOL oxidation on the MWCNT-based samples (substrate-a, C-EC-NP-a, C-EC-NP-R-a, and C-EC-NP-S-a) and the sample holder, respectively.

As discussed above, the electrochemical BINOL oxidation process involved an adsorption step, owing to the affinity between the naphthyl groups of BINOL and the MWCNT surface. Cyclic voltammograms recorded in the BINOL-free electrolyte after linear sweep voltammetry measurements showed that P1 was retained after immersion for 1 h in the BINOL-free electrolyte; however, it disappeared after repeated scanning, whereas P2 was absent. This behavior indicated that BINOL was strongly adsorbed on the MWCNT-based samples but weakly adsorbed on the sample holder (Fig. S22). To facilitate the comparison of P1, which was associated with the MWCNT-based samples, the current was normalized by the maximum current of P2 using the sample holder as an internal reference with no chirality. This normalization corrected minor current fluctuations caused by slight differences in the amount of BINOL supplied to the electrode surface from the bulk electrolyte solution and subsequent adsorption.

We found that the current of P1 depended on the spatial arrangement of BINOL and helicity of the CHNSs. In contrast to the marginal difference in the currents of (*R*)- and (*S*)-BINOL on the substrate-a and C-EC-NP-a electrodes, the P1 current of (*R*)-BINOL was higher than that of (*S*)-BINOL on the C-EC-NP-S-a electrode, whereas the C-EC-NP-R-a electrode showed the opposite trend. The higher and lower P1 current ratios on the C-EC-NP-S-a and C-EC-NP-R-a electrodes were 1.16 and 1.26, respectively (Fig. S23). After correcting for the influence of the sample holder, these values were 1.37 and 1.81, which are comparable to those reported previously for the photoelectrochemical chiral discrimination of BINOL.[46] These values were expected to be identical for the C-EC-NP-S-a and C-EC-NP-R-a electrodes; however, the results deviated from the theoretical behavior. The deviation was attributed to the imperfect mirror-image alignment of the CHNSs on MWCNTs as discussed above and to slight differences in the carbon surface states, including edge-plane exposure and the number of functional groups, which influenced the kinetics of the oxidation reaction.

It should be noted that the binaphthyl compounds used for fabricating the CHNSs and chiral guests had opposite spatial arrangements, suggesting that the binaphthyl compounds functioned as chiral inducers for the helical alignment and the chiral guests fit into the chiral spaces resulting from the alignment. This relationship is different from that observed in the materials synthesized by the chiral imprinting technique.[24–27] Butcha et al.[47] used 3,4-dihydroxyphenylalanine (DOPA) as a chiral imprinting agent to form pores in a Pt–Ir alloy that exhibited excellent chiral discrimination for the corresponding DOPA spatial arrangement. Nevertheless, the carbon material synthesized in this study has the advantages of low cost and a chiral discrimination ability for various compounds.

As an example of the broad applicability of helically aligned fused CHNSs, the chiral discrimination performance was demonstrated for *N,N*-dimethyl-1-ferrocenylethylamine (FcA) in a nonaqueous electrolyte (Fig. S24).[48] Although the retention of FcA in the FcA-free electrolyte was low compared to that of BINOL (Fig. S25), thereby limiting its effect, an FcA-adsorption step might also be involved in the oxidation process.[49,50] The higher/lower current ratios for the FcA oxidation peak on C-EC-NP-S-a and C-EC-NP-R-a were 1.26 and 1.08, respectively. Although these values were lower than those for BINOL, the results indicate the presence of a chiral space in the helically aligned fused CHNSs on MWCNTs that can interact with chiral molecules with specific spatial arrangements (Fig. S26).

Experimental

Materials and Methods

MWCNTs (diameter: 20–40 nm; length: 1–2 μm) were purchased from Tokyo Chemical Industry and used as received. Sodium alginate (300 cps for a 1 wt% aqueous solution, Nacalai Tesque) was used as a carbon binder precursor to prepare a porous MWCNT substrate based on the previously reported strong interaction between sodium alginate and carbon surfaces.[51] Poly(ethylene oxide)/poly(propylene oxide) triblock copolymer (Pluronic F127, Sigma-Aldrich) was used as a dispersant in the substrate preparation process and as a pore-forming agent. EC (STD grade, Industrial, 4 cps, Nisshin Kasei), Fe_3O_4 NP dispersion in toluene (average particle size: 5 nm, 5 wt% including dispersant, Sigma-Aldrich), and (*R*)- and (*S*)-2,2′-bis(methoxymethoxy)-1,1′-binaphthyl (Tokyo Chemical Industry) were used as a carbon source, template, and chiral inducers, respectively. HCl (6 mol dm^{-3}, Nacalai Tesque) was used for acid treatment. High-purity water was obtained by circulating ion-exchanged water through a Barnstead MicroPure water purification system (Thermo Scientific). (*R*)-(+)- or (*S*)-(−)-BINOL (Tokyo Chemical Industry), $LiClO_4$ (Nacalai Tesque), ferrocene (Fc, Nacalai Tesque), and (*R*)-(+)- or (*S*)-(−)-FcA (Tokyo Chemical Industry) were used for electrochemical measurements. A solution of Nafion as a perfluorosulfonate ion-exchange resin [equivalent weight (molar mass/mol of ion-exchange sites) = 1100, 5 wt% in a mixture of lower aliphatic alcohols and 15–20% water] was purchased from Sigma-Aldrich.

Preparation of Porous Substrate

MWCNTs in a dispersed state were fixed in a carbonaceous porous substrate using a carbon binder, and pores were formed via the ice-template method and micelle decomposition. The MWCNT surfaces were treated using a UV/ozone processor (PL16-110, Sen Lights Corporation) to impart hydrophilicity and prepare an aqueous MWCNT dispersion.[52] A 0.75 cm^3 aqueous dispersion was prepared by ultrasonication of 5 mg each of the surface-treated MWCNTs, sodium alginate, and Pluronic F127. After pouring the dispersion into a 15 cm^3 crucible, the bottom of the crucible was immersed in liquid nitrogen to freeze the dispersion, which was then dried under vacuum. Subsequently, the precursor in the crucible was heat-treated at 800 °C for 1 h in an Ar atmosphere to obtain the porous carbon substrate.

Synthesis of Helically Aligned Fused CHNSs on MWCNTs

EC (2.5 mg) and chiral inducer (0.25 mg) were added to 1 cm^3 of the Fe_3O_4 dispersion and mixed well. This starting mixture was poured into the abovementioned crucible containing the substrate. The crucible was covered with a lid and then heated at 30 °C, resulting in the slow evaporation of toluene through small openings between the lid and the rim of the crucible. After solvent evaporation, the complex was dried overnight under a vacuum at 90 °C. Samples obtained using (*R*)- and (*S*)-2,2′-bis(methoxymethoxy)-1,1′-binaphthyl as the chiral inducer (EC-NP-R and EC-NP-S, respectively) were heat-treated at 550 °C for 1 h in an Ar atmosphere to produce the carbonized samples (C-EC-NP-R and C-EC-NP-S, respectively). The EC-NP and C-EC-NP samples were produced using the same method without the chiral inducer. To investigate the effect of the MWCNT substrate, a mixture of ultrasonically dispersed MWCNTs, the Fe_3O_4 NP dispersion, EC, and the chiral inducer, in a similar composition, was slowly dried and carbonized at 550 °C to form a composite. The carbonized samples (C-EC-NP, C-EC-NP-R, and C-EC-NP-S) were treated in boiling 6 mol dm^{-3} HCl for 1 h, thoroughly washed with high-purity water, and dried under vacuum to obtain C-EC-NP-a, C-EC-NP-R-a, and C-EC-NP-S-a, respectively. The substrate before complex formation was subjected to a similar acid treatment to obtain substrate-a.

Characterization

FESEM and TEM images were obtained using JSM-6700F (JEOL) and JEM-2100IM (JEOL) instruments, respectively. For the FESEM observations of EC-NP-R and EC-NP-S, the samples were coated with a thin osmium film using an osmium plasma coater (OPC80T, Filgen). EDX was performed using a JSM-7800F instrument (JEOL). XPS was performed using an AXIS ULTRA DLD system (Kratos Analytical) with Al Ka radiation (1486.6 eV). Raman spectra were collected in backscattering mode using a Raman spectrometer (NRS-5100, JASCO or LabRAM HR Evolution, HORIBA) with a 532 nm laser as the excitation source. The CD measurements for (*R*)-, and (*S*)-2,2′-bis(methoxymethoxy)-1,1′-binaphthyl (0.1 mmol dm^{-3} in ethanol) were performed using a J-820 spectrophotometer (JASCO) with a 0.1 cm cell. The CD spectra of EC, mixtures of EC, and the chiral inducers (EC-R and EC-S) and their intermediate states during carbonization were recorded by fixing the samples on silica glass plates. The starting mixtures with and without the chiral inducer (EC, EC-R, and EC-S) were prepared using 1 cm^3 of toluene instead of the Fe_3O_4 NP dispersion. After dropping 0.1 cm^3 of the mixture on a ⌀2 cm silica glass plate, toluene was evaporated at 30 °C, and the sample was dried under vacuum at 90 °C before being carbonized at 550 °C for 1 h in an Ar atmosphere to yield C-EC, C-EC-R, and C-EC-S. The intermediate states were prepared by increasing the heat treatment temperature to 200, 300, and 400 °C at 5 °C min^{-1}. No substantial dependence of the CD spectra on the plate angle or the process of plate flipping was observed, which confirmed the absence of linear dichroism (LD) and linear birefringence (LB) for these samples.

The pyrolysis behavior of the precursors was analyzed using a thermogravimeter (TG-DSC, STA2500, Netzsch) from 60 to 600 °C at 10 °C min^{-1} under He flow (150 cm^3 min^{-1}). Effluent gas from the TG-DSC measurement was analyzed using a quadrupole mass spectrometer (JMS-Q1500GC, JEOL). N_2 adsorption isotherms were measured at −196 °C using a Belsorp Max II analyzer (MicrotracBEL). From the N_2 adsorption isotherms, specific surface areas were calculated using the Brunauer–Emmett–Teller (BET) method in the pressure range of $P/P_0 = 0.05–0.35$. Pore size distributions were calculated with the nonlocal density functional theory using a slit-pore model.

VUVCD spectroscopy with a wavelength range including the VUV region (~160 nm, the lower limit of the spectrophotometer) was performed using synchrotron radiation as the light source with the VUVCD spectrophotometer at the Hiroshima Synchrotron Radiation Center.[53] The optical devices and sample cells have been described in detail elsewhere.[54,55] A 50-µm-thick polytetrafluoroethylene (PTFE) sheet with a ⌀1.4 cm hole on a ⌀2 cm silica glass plate was used as the substrate for sample fixation. The carbon sample (0.8 mg) was ground and ultrasonically dispersed in 0.2 cm^3 of 2-butanone for 1 min and then fixed on the substrate by dropping 20 mm^3 of the dispersion on the silica plate. Another silica glass plate was placed on the substrate to allow slow solvent evaporation and avoid sample detachment during measurements. After drying, the substrate was assembled in the sample cell equipped with a motorized rotation stage. The incident light beam was perpendicular to the plate. Five spectra were collected by rotating the cell around the beam direction every 22.5°. Five additional spectra at the same angles were measured by flipping the cell, and then these 10 spectra were averaged to minimize the influence of LD and LB.[56–59]

Electrochemical Measurements in an Aqueous System

A three-electrode glass cell and an electrochemical analyzer (ALS760E, BAS) were used for the electrochemical measurements. A sample holder was constructed from ⌀8 mm sheets of porous carbon paper (TGP-H-090, Toray) and the expanded graphite foil (Perma-foil, PF-UHPL, Toyo Tanso) as backing. This sample holder was then sandwiched between two sheets of adhesive PTFE tape with a ⌀6 mm hole in the carbon paper side for exposure to the electrolyte solution and with an Au wire as a lead. The carbon sample (0.25 mg) was sandwiched between the carbon paper and expanded graphite foil to form a working electrode. A glassy carbon (GC) plate polished with 0.05-µm alumina paste (Baikowski), which was ultrasonically cleaned in high-purity water, and subsequently masked using the PTFE adhesive tape with a ⌀6 mm hole was also tested as a working electrode. An activated GC surface (GC-ox) was prepared by surface oxidation in Ar-saturated 0.5 mol dm^{-3} H_2SO_4 at 2.0 V vs. Ag/AgCl/3 mol dm^{-3} NaCl for 30 min as previously reported.[60] Aqueous 3 mol dm^{-3} KOH solution (Ultrapure, Kanto Chemical) was diluted with high-purity water to prepare 0.1 mol dm^{-3} KOH, which was used as the electrolyte with and without 1 mmol dm^{-3} (*R*)-(+)- or (*S*)-(−)-BINOL. To obtain complete electrolyte penetration, before immersing the working electrode in the electrolyte, the pores in the carbon sample were filled with high-purity water by soaking in boiling high-purity water at reduced pressure and room temperature (approximately 23 °C). The counter and reference electrodes were carbon cloth and Hg/HgO/0.1 mol dm^{-3} KOH, respectively. After repeated potential scans between −0.9 and 0.3 V to reach a steady state, cyclic voltammograms were recorded in the Ar-saturated electrolyte without BINOL. Linear sweep voltammograms for BINOL oxidation were collected after immersing the working electrode in the BINOL-containing Ar-saturated electrolyte for 1 h. Thereafter, cyclic voltammograms were recorded in the Ar-saturated electrolyte without BINOL after immersing the working electrode in 0.1 mol dm^{-3} KOH for 1 h.

Electrochemical Measurements in a Nonaqueous System

A ⌀3 mm GC disc was polished with 0.05 µm alumina paste and ultrasonically cleaned in high-purity water for use as a support. The carbon sample (0.2 mg) was ultrasonically dispersed in a mixture of 10 mm^3 of Nafion solution, 90 mm^3 of ethanol, and 100 mm^3 of high-purity water for 30 min. Then, 2 mm^3 of the dispersion was pipetted onto the GC surface and dried overnight at room temperature (approximately 23 °C). The electrolyte was 0.1 mol dm^{-3} $LiClO_4$ dissolved in acetonitrile. Fc, (*R*)-(+)-FcA, and (*S*)-(−)-FcA were used as the redox species at a concentration of 10 mmol dm^{-3}. The counter and reference electrodes were a Pt wire and Ag/Ag$^+$ (10 mmol dm^{-3} AgNO$_3$ + 0.1 mol dm^{-3} tetrabutylammonium perchlorate in acetonitrile), respectively. Linear sweep voltammograms were recorded in the Ar-saturated electrolyte at 25 °C. Thereafter, cyclic voltammograms were recorded in the Ar-saturated 0.1 mol dm^{-3} LiClO$_4$ acetonitrile solution without FcA.

Conclusions

A new form of helical structure was realized in carbon materials, that is, helically aligned fused CHNSs on MWCNTs, which differed from the previously reported twisted-strand-like[11–13] or honeycomb-like porous[14] structures. Helicity was confirmed by VUVCD measurements, and the carbonizing behavior was characterized by TG-DSC-MS measurements to elucidate the generated helicity. The chiral spaces between the CHNSs and MWCNTs, which can interact with chiral molecules, in combination with the electron conductivity and chemical stability of carbon materials, are advantageous for the realization of chiral discriminating electrodes that are usable under a wide range of conditions. The following step in this work involves improving the enantioselectivity. To this end, more precise control of the helical alignment is required, which will lead to the synthesis of suitable samples for clarifying the origins of the CD peaks for helical carbon materials. Such control would also facilitate a more detailed examination of the performance (e.g., sensitivity, repeatability, reliability, and universality) of helically aligned fused CHNSs on MWCNTs as chiral discriminating sensors for enantiomers with different functional groups, chiral centers, molecular weights, and polarities.

Author Contributions

J.M. designed the experiments, synthesized the carbon materials, performed electrochemical measurements, and wrote the manuscript, with input from all authors. M.W. and T.S. also performed electrochemical measurements. N.R., S.M., Y.K., T.N., M.O., K.C., T.Y., and H.N. characterized the carbon materials, precursors, and composites. T.T. performed the carbon surface treatment. K.M. performed VUVCD measurements. F.T. and H.U. provided information about the organic and polymeric raw materials.

Conflicts of interest

There are no conflicts to declare.

Acknowledgements

This study was supported by the NSG Foundation, the Network Joint Research Center for Materials and Devices (no. 20214042), a Grant-In-Aid for Scientific Research (KAKENHI; grant no. 21K05239) from the Japan Society for the Promotion of Science, and JST CREST (grant no. JPMJCR18R3). We would also like to thank Dr. Akagi for helpful discussions.

Notes and references

1 K. Okada, M. Nandi, J. Maruyama, T. Oka, T. Tsujimoto, K. Kondoh and H. Uyama, *Chem. Commun.*, 2011, **47**, 7422.
2 H. Nishihara, T. Hirota, K. Matsuura, M. Ohwada, N. Hoshino, T. Akutagawa, T. Higuchi, H. Jinnai, Y. Koseki, H. Kasai, Y. Matsuo, J. Maruyama, Y. Hayasaka, H. Konaka, Y. Yamada, S.Yamaguchi, K. Kamiya, T. Kamimura, H. Nobukuni and F. Tani, *Nat. Commun.*, 2017, **8**, 109.
3 H. Nishihara and T. Kyotani, *Adv. Mater.*, 2012, **24**, 4473.
4 T. Kyotani, L. -F. Tsai and A. Tomita, *Chem. Mater.*, 1995, **7**, 1427.
5 K. Q. Jian, H. -S. Shim, A. Schwartzman, G. P. Crawford and R. H. Hurt, *Adv. Mater.*, 2003, **15**, 164.
6 T. Kyotani, N. Sonobe and A. Tomita, *Nature*, 1988, 331, 331.
7 A. A. Zakhidov, R. H. Baughman, Z. Iqbal, C. X. Cui, I. Khayrullin, S. O. Dantas, I. Marti and V. G. Ralchenko, *Science*, 1998, **282**, 897.
8 R. Ryoo, S. H. Joo and S. Jun, *J. Phys. Chem. B*, 1999, **103**, 7743.
9 A. Walcarius, *Chem. Soc. Rev.*, 2013, **42**, 4098.
10 J. Wei, Z. Sun, W. Luo, Y. Li, A. A. Elzatahry, A. M. Al-Enizi, Y. Deng and D. Zhao, *J. Am. Chem. Soc.*, 2017, **139**, 1706.
11 M. Kyotani, S. Matsushita, T. Nagai, Y. Matsui, M. Shimomura, A. Kaito and K. Akagi, *J. Am. Chem. Soc.*, 2008, **130**, 10880.
12 S. Liu, Y. Duan, X. Feng, J. Yang and S. Che, *Angew. Chem. Int. Ed.*, 2013, **52**, 6858.
13 C. Zhang, Y. Li, B. Li and Y. Yang, *Chem. Asian J.*, 2013, **8**, 2714.
14 J. Maruyama, T. Shinagawa, M. Watanabe, Y. Kashiwagi, S. Maruyama, T. Nagaoka, W. Matsuda, Y. Tsutsui, S. Seki and H. Uyama, *Small*, 2020, **16**, 1905916.
15 S. Iwama, M. Horiguchi, H. Sato, Y. Uchida, H. Takahashi, H. Tsue and R. Tamura, *Cryst. Growth Des.*, 2010, **10**, 2668.
16 T. Lee and J. F. Peng, *Cryst. Growth Des.*, 2010, **10**, 3547.
17 L. Pu, *Angew. Chem. Int. Ed.*, 2020, **59**, 21814.
18 N. Ousaka, S. Yamamoto, H. Iida, T. Iwata, S. Ito, Y. Hijikata, S. Irle and E. Yashima, *Nat. Commun.*, 2019, **10**, 1457.
19 W. Zou, Y. Yan, J. Fang, Y. Yang, J. Liang, K. Deng, J. Yao and Z. Wei, *J. Am. Chem. Soc.*, 2014, **136**, 578.
20 A. Shundo, K. Hori, T. Ikeda, N. Kimizuka and K. Tanaka, *J. Am. Chem. Soc.*, 2013, **135**, 10282.
21 S. Okur, P. Qin, A. Chandresh, C. Li, Z. Zhang, U. Lemmer and L. Heinke, *Angew. Chem. Int. Ed.*, 2021, **60**, 3566.
22 S. -Y. Zhang, D. Fairen-Jimenez and M. J. Zaworotko, *Angew. Chem. Int. Ed.*, 2020, **59**, 17600.
23 Q. Lin, L. Li and S. Luo, *Chem. Eur. J.*, 2019, **25**, 10033.
24 S. Assavapanumat, T. Yutthalekha, P. Garrigue, B. Goudeau, V. Lapeyre, A. Perro, N. Sojic, C. Wattanakit and A. Kuhn, *Angew. Chem. Int. Ed.*, 2019, **58**, 3471.
25 C. Wattanakit, Y. B. S. Côme, V. Lapeyre, P. A. Bopp, M. Heim, S. Yadnum, S. Nokbin, C. Warakulwit, J. Limtrakul and A. Kuhn, *Nat. Commun.*, 2014, **5**, 3325.
26 J. A. Switzer, H. M. Kothari, P. Poizot, S. Nakanishi and E. W. Bohannan, *Nature*, 2003, **425**, 490.
27 S. Fireman-Shoresh, D. Avnir and S. Marx, *Chem. Mater.*, 2003, **15**, 3607.
28 Y. Jiao, D. Han, L. Liu, L. Ji, G. Guo, J. Hu, D. Yang and A. Dong, *Angew. Chem. Int. Ed.*, 2015, **54**, 5727.
29 G. Singh, H. Chan, A. Baskin, E. Gelman, N. Repnin, P. Král and R. Klajn, *Science*, 2014, **345**, 1149.
30 M. -A. Moradi, E. D. Eren, M. Chiappini, S. Rzadkiewicz, M. Goudzwaard, M. M. J. van Rijt, A. D. A. Keizer, A. F. Routh, M. Dijkstra, G. de With, N. Sommerdijk, H. Friedrich and J. P. Patterson, *Nat. Mater.*, 2021, **20**, 541.
31 Z. -Z. Pan, A. Govedarica, H. Nishihara, R. Tang, C. Wang, Y. Luo, W. Lv, F. -Y. Kang, M. Trifkovic and Q. -H. Yang, *Small*, 2021, **17**, 2005564.
32 D. M. Applin, M. R. M. Izawa, E. A. Cloutis, J. J. Gillis-Davis, K.

M. Pitman, T. L. Roush, A. R. Hendrix and P. G. Lucey, *Icarus*, 2018, **307**, 40.

33 G. A. Rance, D. H. Marsh, R. J. Nicholas and A. N. Khlobystov, *Chem. Phys. Lett.*, 2010, **493**, 19.

34 R. Kuzuo, M. Terauchi and M. Tanaka, *Jpn. J. Appl. Phys.*, 1992, **31**, L1484.

35 S. Che, Z. Liu, T. Ohsuna, K. Sakamoto, O. Terasaki and T. Tatsumi, *Nature*, 2004, **429**, 281.

36 X. Lan, X. Lu, C. Shen, Y. Ke, W. Ni and Q. Wang, *J. Am. Chem. Soc.*, 2015, **137**, 457.

37 A. Sadezky, H. Muckenhuber, H. Grothe, R. Niessner and U. Pöschl, *Carbon*, 2005, **43**, 1731.

38 F. Jaouen, F. Charreteur and J. P. Dodelet, *J. Electrochem. Soc.*, 2006, **153**, A689.

39 Z. Mo, X. Zhu, G. Wang, W. Han and R. Guo, *J. Mater. Res.*, 2014, **29**, 2156.

40 E. Billiot, J. Macossay, S. Thibodeaux, S. A. Shamsi and I. M. Warner, *Anal. Chem.*, 1998, **70**, 1375.

41 J. Zhang, L. Gong, K. Sun, J. Jiang and X. Zhang, *J. Solid State Electrochem.*, 2012, **16**, 2179.

42 D. S. Jeong, J. M. Yun and K. -H. Kim, *RSC Adv.*, 2017, **7**, 44735.

43 Z. Wang, F. Yang, H. Zheng, X. Qin, J. Luo, Y. Li and D. Xiao, *Analyst*, 2014, **139**, 3622.

44 A. J. S. Ahammad, S. Sarker, M. A. Rahman and J. -J. Lee, *Electroanalysis*, 2010, **22**, 694.

45 H. Qi and C. Zhang, *Electroanalysis*, 2005, **17**, 832.

46 H. Junxiang, H. Sato, Y. Umemura and A. Yamagishi, *J. Phys. Chem. B*, 2005, **109**, 4679.

47 S. Butcha, S. Assavapanumat, S. Ittisanronnachai, V. Lapeyre1, C. Wattanakit and A. Kuhn, *Nat. Commun.*, 2021, **12**, 1314.

48 M. Longhi, S. Arnaboldi, E. Husanu, S. Grecchi, I. F. Buzzi, R. Cirilli, S. Rizzo, C. Chiappe, P. R. Mussini and L. Guazzelli, *Electrochim. Acta*, 2019, **298**, 194.

49 N. Kurapati, P. Pathirathna, R. Chen and S. Amemiya, *Anal. Chem.*, 2018, **90**, 13632.

50 A. S. Cuharuc, G. Zhang and P. R. Unwin, *Phys. Chem. Chem. Phys.*, 2016, **18**, 4966.

51 I. Kovalenko, B. Zdyrko, A. Magasinski, B. Hertzberg, Z. Milicev, R. Burtovyy, I. Luzinov and G. Yushin, *Science*, 2011, **334**, 75.

52 F. Morales-Lara, M. J. Pérez-Mendoza, D. Altmajer-Vaz, M. García-Román, M. Melguizo, F. J. López-Garzón and M. Domingo-García, *J. Phys. Chem. C*, 2013, **117**, 11647.

53 K. Matsuo, M. Kumahiro and K. Gekko, *Chirality*, 2020, **32**, 594.

54 N. Ojima, K. Sakai, K. Matsuo, T. Matsui, T. Fukazawa, H. Namatame, M. Taniguchi and K. Gekko, *Chem. Lett.*, 2001, **30**, 522.

55 K. Matsuo, K. Sakai, Y. Matsushima, T. Fukuyama and K. Gekko, *Anal. Sci.*, 2003, **19**, 129.

56 J. Bürck, P. Wadhwani, S. Fanghänel and A. S. Ulrich, *Acc. Chem. Res.*, 2016, **49**, 184.

57 G. Albano, M. Górecki, G. Pescitelli, L. D. Bari, T. Jávorfi, R. Hussain and G. Siligardi, *New J. Chem.*, 2019, **43**, 14584.

58 M. Tanaka, K. Yagi-Watanabe, F. Kaneko and K. Nakagawa, *J. Phys. Chem. A*, 2010, **114**, 11928.

59 J. -i. Takahashi, H. Shinojima, M. Seyama, Y. Ueno, T. Kaneko, K. Kobayashi, H. Mita, M. Adachi, M. Hosaka and M. Katoh, *Int. J. Mol. Sci.*, 2009, **10**, 3044.

60 J. Maruyama and I. Abe, *Electrochim. Acta*, 2001, **46**, 3381.